applied optics

# Development of space active optics for a whiffletree supported mirror

Pingwei Zhou,[1,2,*] Dongxu Zhang,[1] Guang Liu,[2] and Changxiang Yan[1]

[1]Changchun Institute of Optics, Fine Mechanics and Physics, Chinese Academy of Sciences, Changchun 130033, China
[2]University of Chinese Academy of Sciences, Beijing 100039, China
*Corresponding author: npuzhoupw@163.com

Received 26 April 2019; revised 19 June 2019; accepted 19 June 2019; posted 20 June 2019 (Doc. ID 366125); published 17 July 2019

**The requirements of a lightweight primary mirror for large-aperture space telescopes include a precise mirror figure and high reliability. However, lightweight mirrors are easily affected by environmental disturbances, as they lack structural stability and rigidity. Active optics can be used to compensate for the gravity-induced deformation and correct low-order aberrations due to thermal changes and gravity relief during observing periods. Due to their complexity, active optics have been rarely used in space. To validate the technology of space active optics, an active optics system based on a passive, whiffletree-supported mirror is developed. During integration and testing on ground and under normal conditions in space, the surface accuracy is guaranteed by passive support. Within this hybrid support, the active optics system only serves to assist support. This paper focuses on the compatibility between a passive multisupporting system and active optics. We present the prototype of a 0.676 m diameter passive supported lightweight mirror and active support with nine axial force actuators. The passive support includes a 9-point axial support and three A-frame lateral support. The active actuator distribution has been optimized with finite element analysis and its experimental performance characterized in representative conditions. The effectiveness of the hybrid passive–active support developed has been verified.** 

https://doi.org/10.1364/AO.58.005740

## 1. INTRODUCTION

Astronomical and Earth observations performed using space telescopes have become increasingly common in recent years. Space observation has many advantages, including the avoidance of the effects of weather and image fluctuations due to atmospheric turbulence. It also enables observation in wavelengths blocked by Earth's atmosphere, thereby offering more information than Earth-based observations [1]. High resolution implies larger space telescopes, which have been constrained by carrying capacity of available launch vehicles. To solve this problem, several concepts have been studied and tested [2–6]. The James Webb Space Telescope, adopting a folding primary mirror, is currently under construction. This is a major step forward in space telescope technology, although the cost and complexity associated with folding mirror architectures will ultimately necessitate simpler and more effective approaches. The maturity level of the other proposals, which require in-orbit self-assembly or thin mirrors, is still far from application. At the current stage, building space telescopes under 6 m can still employ a monolithic lightweight primary mirror and active optics to satisfy optical requirements throughout the mission lifetime. The Hubble 2.4 m primary mirror was supported by passive support and 24 axial actuators of which the layout was designed to correct astigmatism [7]. As only spherical aberration induced by incorrect fabrication was found in space, the active optics system has not been used. Although today the active optics is a basic technology in astronomy, it has not been fully validated in space.

In this paper, we present the prototype of a 0.676 m diameter passive supported lightweight mirror and active support with nine axial force actuators. The passive support includes a 9-point axial support and three A-frame lateral support. During integration and testing on ground and under normal conditions in space, the surface accuracy is guaranteed by passive support. Within this hybrid support, the active optics system only serves to assist support. In this way, the technology of space active optics can be validated and prepared for future application. This paper has focused on the compatibility between passive multisupporting system and active optics. Meanwhile, the active actuator distribution has been optimized with finite element analysis and its experimental performance characterized in representative conditions. The effectiveness of the hybrid passive–active support developed has been verified.

## 2. SUPPORT SYSTEM OVERVIEW

In this system, a monolithic SiC primary mirror (PM) with a partially closed back is examined. Some advantages of the partially closed back design include higher mirror flexural rigidity

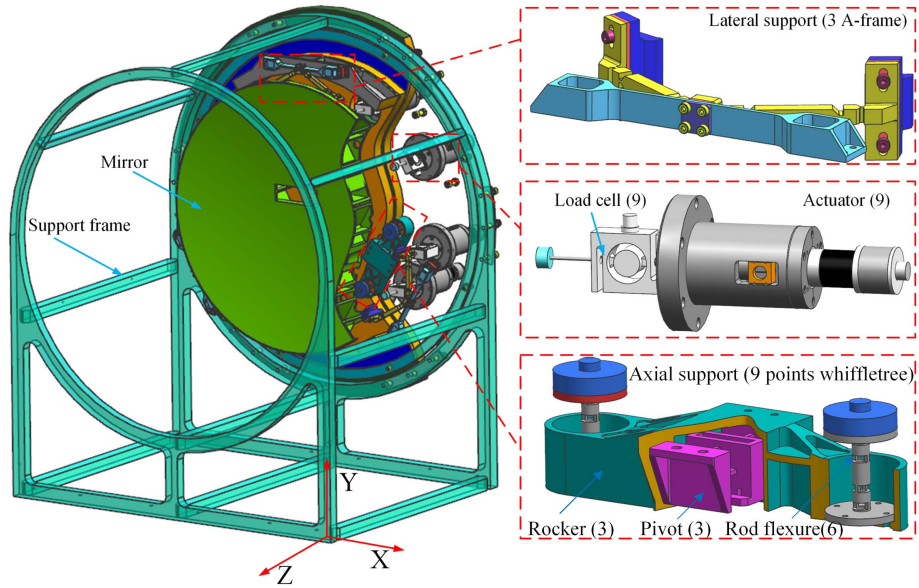


**Fig. 1.** 0.676 m SiC lightweight mirror assembly showing the support frame, mirror body, passive support, and active support. For clarity, part of the model has been cut off along the wave lines.

relative to open-back designs and fabrication simplicity relative to built-up configurations. The aperture diameter is 0.676 m, the radius of curvature is 1.91 m, the thickness is 0.07 m, and the mass is 25 kg. The side length of the triangular isogrid is 0.09 m, and the intersections have a 0.026 m inscribed circle diameter. This spherical mirror was once the backup mirror of a coaxial optical telescope, which was supported by three points. To develop the prototype of multipoint supports and active optics, the mirror has been modified as shown in Fig. 1. The passive support employs a 9-point whiffletree for axial constraint (piston, tip, and tilt DOFs) and a set of three A-frame supports for lateral support (two in-plane and one clocking DOFs) [8]. The whiffletrees include a stiff rocker, flexural pivots, rod flexure, and invar interface pads bonded between the flexure and the mirror. The A-frame is composed of tangent flexure, bipod, and invar bonding blocks. The flexures are made from titanium for dimensional stability. The active optics system includes nine actuators of which the distribution has been optimized for astigmatism and trefoil in Section 2. The material properties used in the primary mirror assembly are summarized in Table 1.

**Table 1. Material Properties Used in the Primary Mirror Assembly**

| Material | SiC (Mirror) | Invar (Interface) | Titanium (Flexure) | Adhesive |
|---|---|---|---|---|
| Young's modulus (GPa) | 390 | 141 | 109 | 0.158 |
| Poisson's ration | 0.25 | 0.25 | 0.29 | 0.49 |
| Density (t/mm3) | $3.05 \times 10^{-9}$ | $8.1 \times 10^{-9}$ | $4.4 \times 10^{-9}$ | $1.3 \times 10^{-9}$ |
| Coefficient of thermal expansion (/°C) | $2.5 \times 10^{-6}$ | $2.5 \times 10^{-6}$ | $9.1 \times 10^{-6}$ | $3 \times 10^{-3}$ |

## 3. AXIAL ACTUATOR DISTRIBUTION OPTIMIZATION

A set of 33 candidate low-stiffness force actuator locations, which are the strut intersections for structural efficiency, is shown in Fig. 2. These actuators are intended to be push–pull-style force actuators acting along the optical axis. Considering the weight and power consumption, it was desired to find the optimum layout, which uses a total of nine actuators. In the active optics system, the passive axial support can serve as three hard points. Based on the PM's free-free modal analysis and deformation data from flying telescopes [4], the Zernike terms Z5 (primary astigmatism at 0°), Z6 (primary astigmatism at 45°), Z10 (primary trefoil at 0°), and Z11 (primary trefoil at 30°) are chosen to be the goal of optimization. Basically, the in-space aberrations come from the thermal gradients as well as the gravity difference between the integration on Earth and the operations in space.

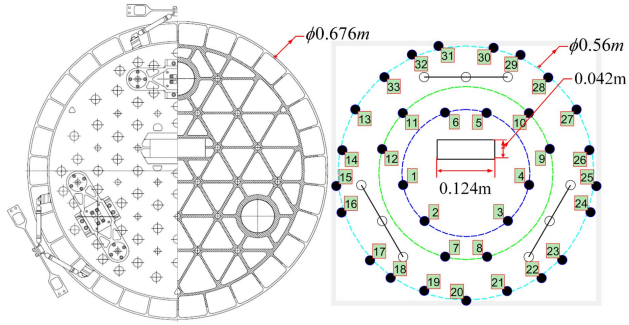


**Fig. 2.** Half-section view shows the passive support and candidate actuator locations, which are the strut intersections for structural efficiency. Solid black circles represent the candidate actuator; white circles represent the support points and the pivots of the whiffletree.

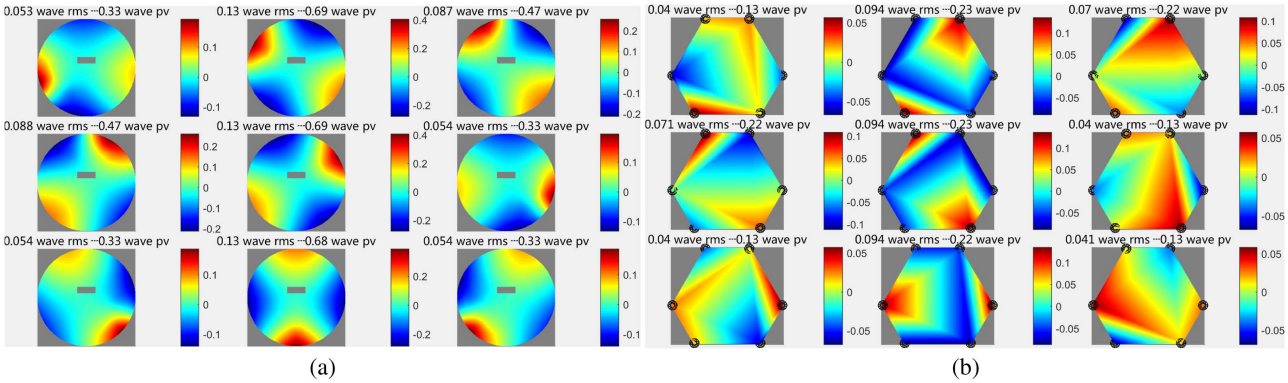


**Fig. 3.** After optimization, the adopted nine influence functions under 100N expected from FEA in which the piston and tilt have been removed. (a) $IF_S$ (b) $IF_I$ in which the black circles represent the nodes located at the invar interface pads of whiffletree support.

An influence function of the mirror surface ($IF_S$) represents the effect of one actuator under unit load on the mirror surface. When performing finite element analysis, the evaluated aperture is 0.67 m. Figure 3(a) shows the finally selected nine actuator locations' $IF_S$, which are used to compare with those of measurement. The unit load not only deforms the mirror surface but also the interface between the mirror and passive whiffletree support, as shown in Fig. 3(b). To define the piston and tilt DOF of the PM, a reference plane is created at the location of the nine bonding interfaces. Similarly, the Interface influence function ($IF_I$) represents the deformation of the nine bonding interfaces with respect to the reference plane under unit load of one actuator. Two conditions must be met in order to decouple the active and passive support. First, the applied active force has to maintain force and moment equilibrium. Second, when the active system is working, the rigid motion of the primary mirror assembly is not allowed. The PM's rigid motion is defined by the interface influence functions. With 33 candidate actuator locations, the studied system has two sets of 33 IFs. As nine actuators are needed, the random combination of nine actuators' IFs constitute characteristic base A, which is used to decompose the aberrations $[\delta_{\mathrm{Ast0}}, \delta_{\mathrm{Ast45}}, \delta_{\mathrm{Tre0}}, \delta_{\mathrm{Tre30}}]$:

$$\delta_d = \begin{bmatrix} \delta_{\mathrm{Ast0}} & \delta_{\mathrm{Ast45}} & \delta_{\mathrm{Tre0}} & \delta_{\mathrm{Tre30}} \\ 0_{\mathrm{size}(\mathrm{IF}_I)} & 0_{\mathrm{size}(\mathrm{IF}_I)} & 0_{\mathrm{size}(\mathrm{IF}_I)} & 0_{\mathrm{size}(\mathrm{IF}_I)} \end{bmatrix} = A\alpha = \begin{bmatrix} \mathrm{IF}_S \\ \mathrm{IF}_I \end{bmatrix} \alpha, \tag{1}$$

where $\delta_d$ is the deformation of the mirror surface and the bonding interface between mirror and whiffletree support. $\alpha$ is four sets of nine coefficients corresponding to the applied actuator force.

These coefficients are determined by computing the generalized inverse of influence functions base under the condition of force and moment equilibrium:

$$\begin{cases} \alpha = (A^t A)^{-1} A^t \delta_d \\ \text{s.t.} \begin{bmatrix} F_Z \\ M_X \\ M_Y \end{bmatrix} = \begin{bmatrix} \mathrm{ones}_{1\times 9} \\ Y_{\mathrm{Act}} \\ -X_{\mathrm{Act}} \end{bmatrix} \alpha = 0 \end{cases}, \tag{2}$$

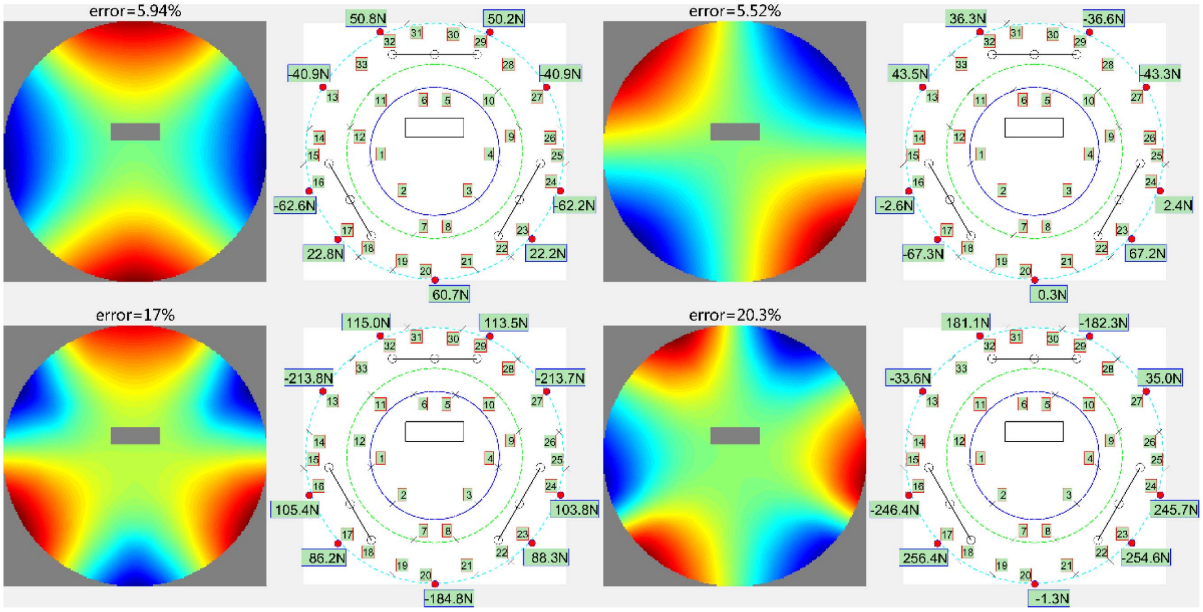


**Fig. 4.** Optimal result showing the residual rms deviation obtained from MATLAB, the distribution of actuators, and the computed active force.

where $X_{\mathrm{Act}}$ and $Y_{\mathrm{Act}}$ are the coordinates of the selective nine actuators along the $X$ and $Y$ axes, respectively.

Thus, the mirror surface actually produced or compensated by the system is

$$\delta_{\mathrm{cor}} = A(A^t A)^{-1} A^t \delta_d. \tag{3}$$

When correcting the desired aberration, some other higher aberrations may be introduced. Thus, we take the residual rms ratio as the optimizing target. In this paper, MATLAB is used to superimpose influence functions and rms calculation. The automatic optimization platform for the axial actuator distribution is established based on the multidisciplinary optimization software Isight. The multiobjective nondominated sorting genetic algorithm [9] (NSGA-II) is adopted to optimize the distribution to minimize the target. We built 33-bit variables equal to the number of candidate actuators in which a "1" indicates the actuator is included for correction, while a "0" indicates that it is not [10]. The sum of the 33 digit variables is set to be 9. For each prescribed aberration, a least-squares fit with constraints is performed to minimize the residual rms ratio using a linear combination of the actuator influence functions. Figure 4 shows the prediction of the correction capacity of wave/2 (wave = 632.8 nm) along with the amplitudes of the required actuator inputs. The final optimized point selected from the Pareto solutions has a minimum residual rms ratio for astigmatism. The maximum percentages of residual rms deviation for astigmatism and trefoil are 5.94% and 20.3%, respectively. Comparing with astigmatism correction, correcting trefoil introduces more high-order aberrations, and the required active force is almost four times larger. Then, we applied the computed active force back to the FEA model to check if the two conditions mentioned above have been satisfied. The result is shown in Fig. 5 in which the piston and tilt have not been removed. The Zernike coefficients [11] of the four optimized aberrations are −0.4794 wave, −0.4802 wave, −0.4666 wave, and −0.4609 wave, respectively, and close to the target of 0.5 wave. Meanwhile, the rigid Zernike terms show that no rigid motion has appeared.

## 4. INFLUENCE FUNCTIONS

### A. Influence Function Test

The axial actuators incorporate brushless DC motors with gear planetary reducers and an acme thread leadscrew to reduce cost and size [12]. The assembled actuator is shown in Fig. 1 and includes an S-shaped load cell for a local force control loop. The titanium rod flexure is used to provide high stiffness in the axial direction while providing compliance in all other degrees of freedom. This flexure is attached to an invar interface pad, providing the final mating surface to the primary mirror. We have measured that the force accuracy and load capacity are less than 0.1N and ±350N (pull and push). Meanwhile, tests of long-term stability indicate a force drift of less than ±3 mN. A screen image of the control panel for actuators is shown in Fig. 7. The graphical user interface allows users to input the computed active forces, start and stop open- and closed-loop of the actuators in parallel, and read actuator positions in real time.

A Fizeau interferometer, as shown in Fig. 6, is used to measure the optical surface deformation. The mirror is tested horizontally due to simplicity and ease of implementation. The repeatability of the PM WFE measurements has been evaluated using five back-to-back measurements, each an average of 300. The maximum difference in the RMS wavefront error (WFE) of each measurement from the average of the five measurements was 1/500 wave and is well within the allotted uncertainty. Figure 8(a) represents the initial wavefront error (WFE) without active force and with piston, tilt, and focus Zernike terms removed. This measured result is mostly comprised of fabrication error, assembly error, and deflection under self-weight. The decomposition using 37-term Zernike polynomials fit is shown in Fig. 8(b). It is found that the Zernike term Z6 (astigmatism at 45°), Z7 (X coma), and Z10 (trefoil at 90°) are relatively high in which Z7 can be corrected by adjusting the position of the secondary mirror assembly using Hexapod [13]. Due to misalignment of the interferometer and change in the radius of primary mirror before and after applying active force, the image size and position at CCD are different. As the IF test is on the basis of the initial PM WFE, the IF is

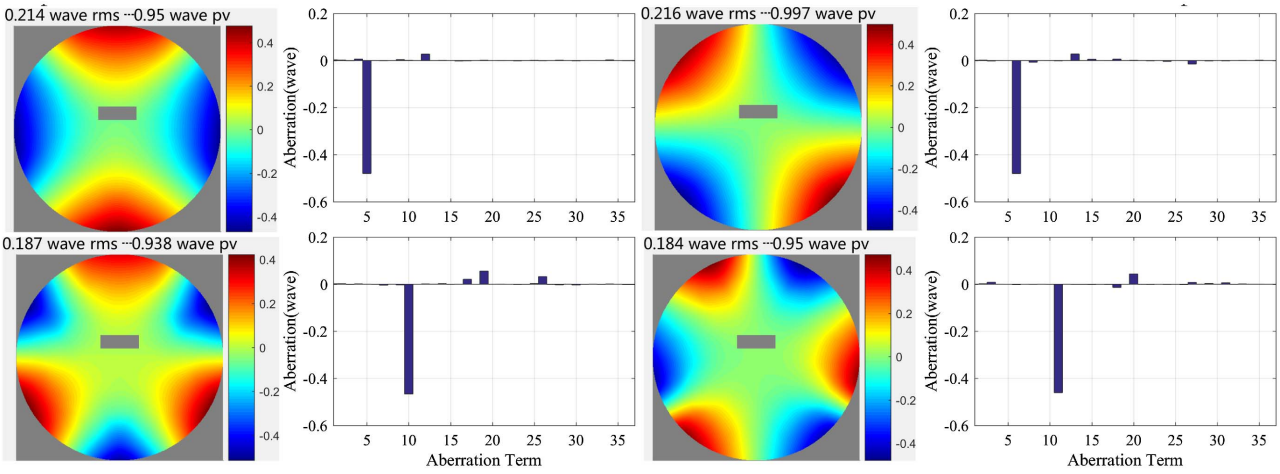


**Fig. 5.** Four generated aberrations expected from FEA in which the piston and tilt have not been removed and 37-term fringe Zernike polynomials decomposition (wave = 632.8 nm).

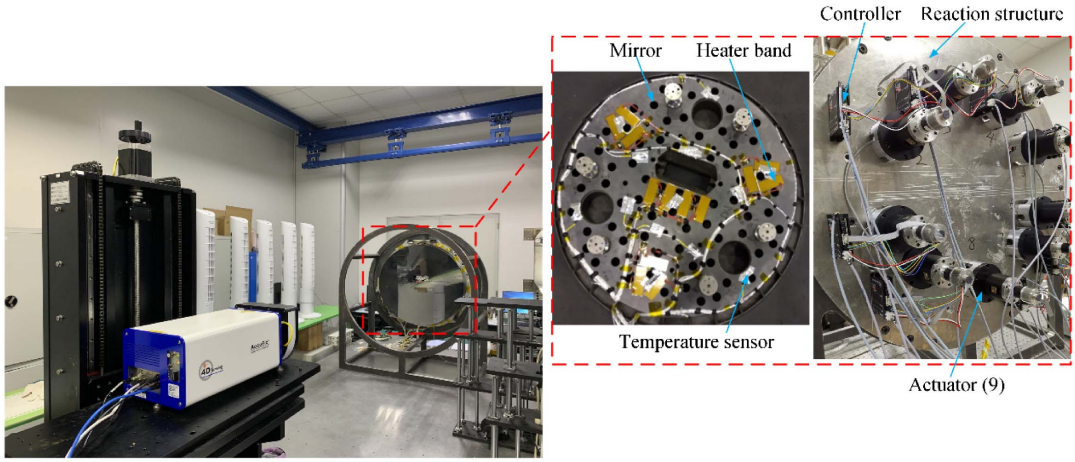


**Fig. 6.** Integrated system on its test platform showing the experimental apparatus of heat and active optics.

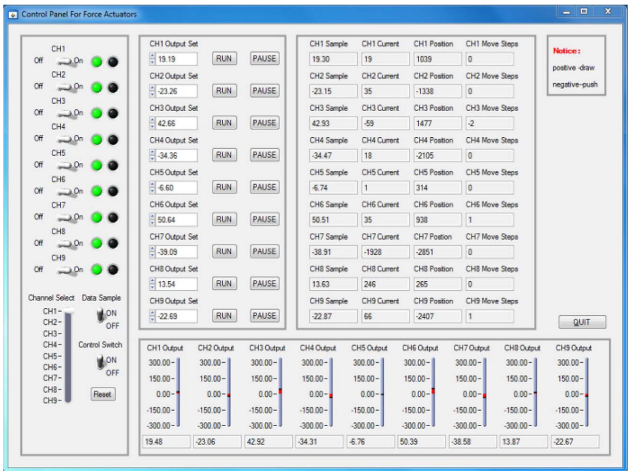


**Fig. 7.** Screen image of force control panel.

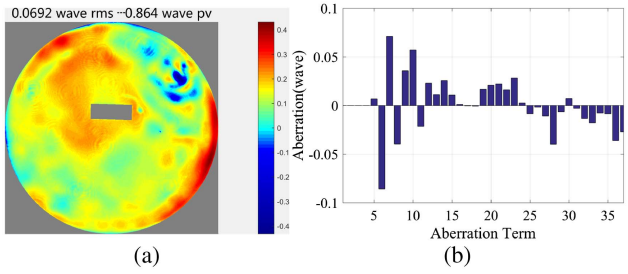


**Fig. 8.** (a) Measured mirror surface accuracy using optical interferometer before active optics test in which the piston, tilt, and focus have been removed. (b) The 37-term fringe Zernike polynomials decomposition.

obtained by subtracting the initial WFE after alignment and scale using bilinear interpolation.

The nine $IF_S$ are measured by applying a 100N push to each actuator while the others are put at zero. The recovered $IF_S$ shown in Fig. 9 are compared with the ones expected from

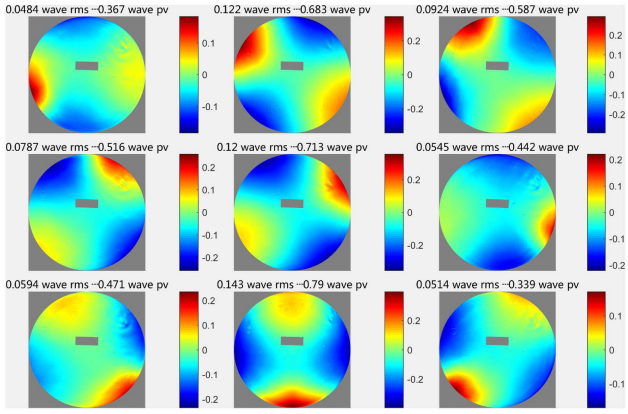


**Fig. 9.** Influence functions of mirror surface in which the piston and tilt have been removed, measured with a Fizeau interferometer.

FEA shown in Fig. 3. As we can see in Figs. 3 and 9, their shapes are similar, and the difference comes from their amplitudes. Figure 10 shows the ratios of the amplitudes, which fall in the interval between 0.9 and 1.1. The inconsistency and variation of ratios are mainly resulting from the machining error of SiC mirror.

### B. Zernike Mode Correction

As the IF of interface $IF_I$ cannot be directly measured, the $IF_I$ obtained from FEA is used after scaling based on the ratios shown in Fig. 10. Before computing the active force, a 37-term Zernike fit is applied to reduce high-frequency noise of the measured $IF_S$. Figure 11 shows the computed active force to generate the four prescribed aberrations of a 0.5 wave. The maximum forces are 75.7N, 87.8N, 327.5N, and 258.5N, respectively. As the load capacity of the designed actuator is 350N, the Z5, Z6, Z10, and Z11 terms can be generated at amplitudes around 2.3 wave, 2 wave, 0.53 wave, and 0.68 wave accordingly. The measured result is shown in Fig. 12. It can be seen that the astigmatism is well corrected and that the trefoil is less well corrected just as predicted as FEA. The difference in Zernike coefficient and rms is listed in Table 2. The variation of the PM piston and tilt, calculated from the measured PM

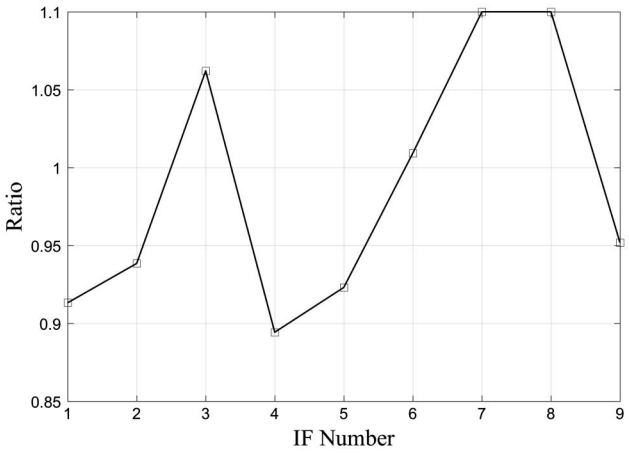


**Fig. 10.** Ratios of the amplitude of IFs between measurement and FEA.

WFE, is also listed in Table 2. Compared with the piston and tilt of initial PM WFE, the maximum difference in the prescribed aberrations is 0.14 μm and 0.58 in., respectively. These results are consistent with expectations.

### C. Gravity Correction

In Section 4.B, the capacity for correcting single Zernike modes has been tested and verified. The deformation induced by gravity and thermal change can be considered as a random combination of Zernike modes. It is difficult to predict or realize the in-space aberrations, which mainly come from gravity relief and thermal change. The correction tests in this section are just an example of the corresponding shapes deformed by environmental factors. The initial PM WFE is shown in Fig. 8(a). Although the actuator layout has been optimized for astigmatism and trefoil, all the Zernike terms shown in Fig. 8(b) have been corrected to minimize the surface deformation. Figure 13(a) shows the computed active force in which the maximum force is 50.6N. The residual rms after compensation is 0.0589 wave, as shown in Fig. 13(b), which accounts for 85% of that shown in Fig. 8(a). As shown in Fig. 13(c), the Zernike terms Z6 and Z10 have been corrected effectively. The value of Zernike term Z7 has not changed because the nine actuators are almost distributed in a circle while the radial order of Z7 is 3. Based on aberration theory, Z7 can be corrected by adjusting the position of the secondary mirror assembly using Hexapod.

**Table 2. Summary of Measured Performance of Single Zernike Term**

| Zernike term | Z5 (0.5λ) | Z6 (0.5λ) | Z10 (0.5λ) | Z11 (0.5λ) |
|---|---|---|---|---|
| Piston/μm | 0.07 | 0.14 | 0.025 | 0.023 |
| Tilt X/″ | −0.38 | −0.28 | −0.55 | −0.56 |
| Tilt Y/″ | 0.58 | 0.14 | −0.14 | 0.052 |
| Coefficient difference | −4.14% | 3.02% | 10% | 4.32% |
| RMS difference | −2.5% | 4.85% | 3.85% | 9.16% |

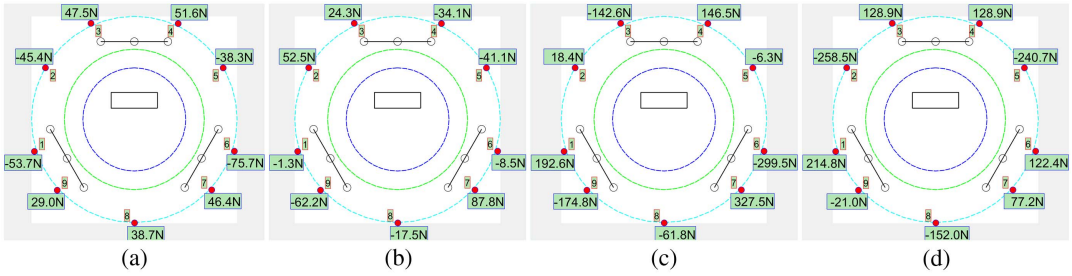


**Fig. 11.** Computed active force using measured $IF_S$ and scaled $IF_I$.

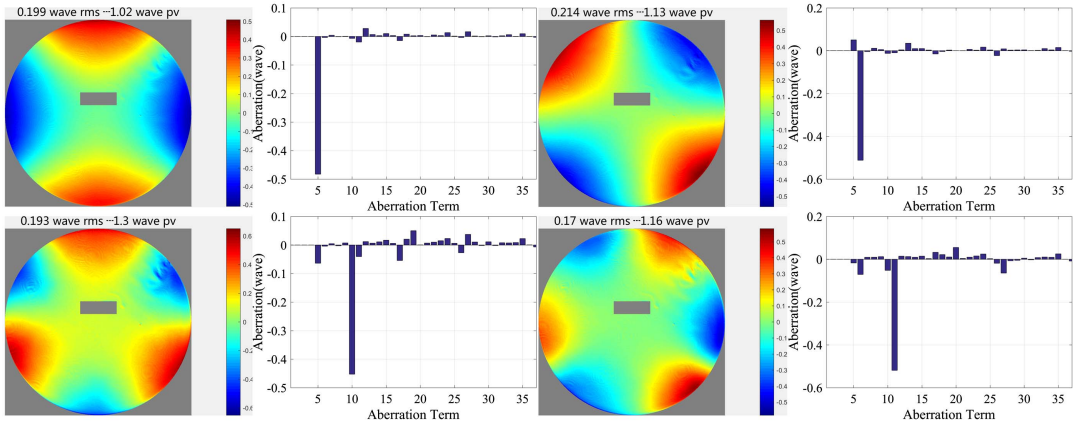


**Fig. 12.** Measured Zernike modes of astigmatism and trefoil in which piston and tilt have not been removed.

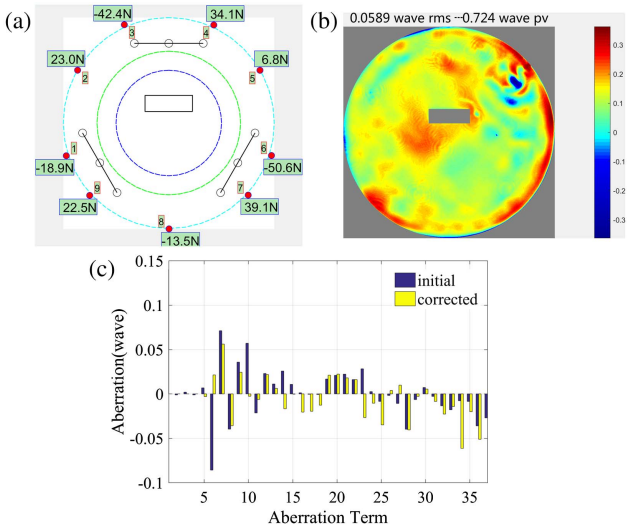


**Fig. 13.** (a) Computed active force for correcting initial PM WFE. (b) The measured PM WFE after correction in which the piston, tilt, and focus have not been removed. (c) The 37-term fringe Zernike polynomials decomposition.

### D. Thermal Correction

Given the variety of potential thermal disturbances and the many factors that affect the thermal control system during a mission, there are myriad of potential thermal cases to consider [14]. As the complicated thermal cases can often be decomposed into the simple cases of uniform temperature change, axial temperature gradient, and radial temperature gradient, the central heater zone is warmed up to produce the three thermal cases simultaneously. Figure 14 shows the measured thermal distribution of the PM assembly by using the temperature sensors. It can be seen that there is 4.5 deg temperature rise and 1.52 deg axial gradient. In addition, the radial gradients at the PM back and front are 2.4 and 1.52 deg, respectively. The measured PM WFE resulting from thermal change is shown in Fig. 15(a) in which initial WFE shown in Fig. 8(a) has been subtracted with piston, tilt, and defocus removed. As shown in Fig. 15(a), there are hotspots on the mirror surface due to the flow disturbance, which is probably resulting from the instability of the temperature control system. We

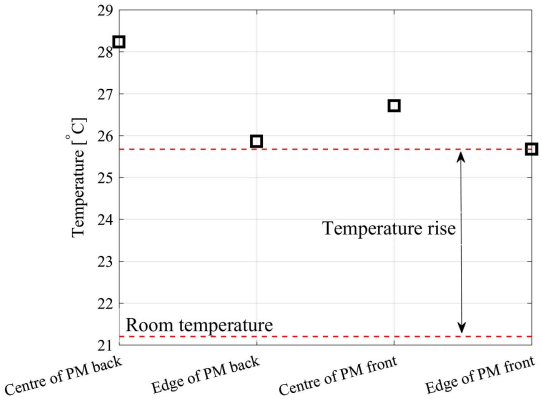


**Fig. 14.** Measured thermal distribution of PM assembly.

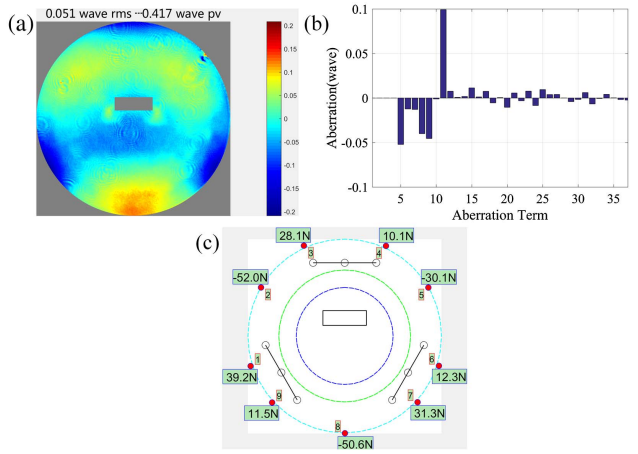


**Fig. 15.** (a) Measured PM WFE resulting from thermal change in which the piston, tilt, and focus have been removed. (b) The 37 terms fringe Zernike polynomials decomposition. (c) The computed active force for correcting PM WFE induced by thermal change.

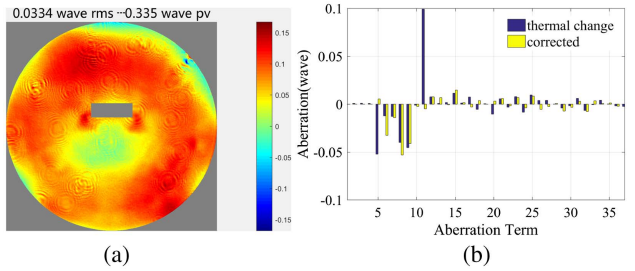


**Fig. 16.** (a) Measured PM WFE after correction in which the piston and tilt have not been removed. (b) The 37 terms fringe Zernike polynomials decomposition.

are currently improving the stability of the temperature control system in order to reduce the flow disturbance. The defocus can easily be removed by on-orbit realignment of telescopes. The dominant Zernike term except the defocus term is Z11 of 0.1 wave, as shown in Fig. 15(b). After applying the active force shown in Fig. 15(c), the residual rms after compensation is 0.0334 wave, as shown in Fig. 16(a), which accounts for 65.6% of that shown in Fig. 15(a). As shown in Fig. 16(b), the Zernike term Z11 has been corrected effectively.

## 5. CONCLUSION

To validate the technology of space active optics, we presented the prototype of a 0.676 m diameter passive supported lightweight mirror and active support with nine axial force actuators. Within the hybrid support, the active support only served to assist support. During integration and testing on ground and under normal conditions in space, the surface accuracy was guaranteed by passive support. The distribution of force actuators has been optimized to maximize the correction capacity for astigmatism and trefoil. To characterize the system, the influence functions of the primary mirror assembly have been measured. Also, the ratios of the amplitudes between measurement

and FEA fell in the interval between 0.9 and 1.1. From those characteristics, the correction capabilities have been determined for Z5, Z6, Z10, and Z11. The Z5 and Z6 were easily generated at amplitudes around 2.3 wave and 2 wave, and the Z10 and Z11 could be corrected up to 0.53 wave and 0.68 wave due to the mirror's structural rigidity and actuator's force limit. When generating the above aberrations of the 0.5 wave, the maximum piston and tilt were 0.14 μm and 0.58 in., respectively. From these results, the compatibility and effectiveness of the hybrid support have been verified. To determine the correction capacity for combined Zernike terms and representative conditions, the cases of gravity and thermal change have also been corrected. After correction, the Zernike terms Z5, Z6, Z10, and Z11 have been reduced simultaneously, and the PM WFEs have been improved 15% and 34.5%, respectively. Those results are promising for the application of such a hybrid support to compensate the unexpected deformations and validate the space active optics.

**Funding.** National Natural Science Foundation of China (NSFC) (61705223).

## REFERENCES

1. M. Kotani, T. Imai, H. Katayama, H. Kaneda, T. Nakagawa, and K. Enya, "Quality evaluation of spaceborne SiC mirrors (I): analytical examination of the effects on mirror accuracy by variation in the thermal expansion property of the mirror surface," Appl. Opt. **52**, 4797–4805 (2013).
2. M. Postman, T. Brown, K. Sembach, M. Giavalisco, and W. Traub, "Advanced technology large-aperture space telescope: science drivers and technology developments," Opt. Eng. **51**, 011007 (2012).
3. N. Devaney, F. Kenny, A. V. Goncharov, M. Goy, and C. Reinlein, "Development of a prototype active optics system for future space telescopes," Appl. Opt. **57**, E101–E106 (2018).
4. M. Laslandes, C. Hourtoule, E. Hugot, M. Ferrari, C. Lopez, C. Devilliers, and F. Chazallet, "Space active optics: performance of a deformable mirror for in-situ wave-front correction in space telescopes," Proc. SPIE **8442**, 844220 (2012).
5. C. Atkinson, S. Texter, R. Keski-Kuha, and L. Feinberg, "Status of the JWST optical telescope element," Proc. SPIE **9904**, 990403 (2016).
6. J. T. Mooney, P. J. Reardon, D. Gregory, A. Manning, J. B. Blackmon, T. Howsman, P. Williams, W. Brantley, J. M. Rakoczy, K. Herren, D. Tucker, and A. Sharma, "Novel in-space manufacturing for the development of large space telescopes," Proc. SPIE **6265**, 62652W (2006).
7. M. D. Lallo, "Experience with the Hubble Space Telescope: 20 years of an archetype," Opt. Eng. **51**, 011011 (2012).
8. H. Bittner, M. Erdmann, P. Haberler, and K. H. Zuknik, "SOFIA primary mirror assembly: structural properties and optical performance," Proc. SPIE **4857**, 458636 (2003).
9. H. An, D. E. Green, and J. Johrendt, "Multi-objective optimization and sensitivity analysis of tube hydroforming," Int. J. Adv. Manuf. Technol. **50**, 67–84 (2010).
10. G. J. Michels, V. L. Genberg, K. B. Doyle, and G. R. Bisson, "Design optimization of actuator layouts of adaptive optics using a genetic algorithm," Proc. SPIE **5877**, 58770L (2005).
11. D. Malacara, "Zernike polynomials and wavefront fitting," in *Optical Shop Testing* (Wiley, 2007), pp. 298–545.
12. X. Cui, Y. Li, X. Ni, D. Yang, Z. Q. Yao, G. Li, and Y. Wang, "Active support system of LAMOST reflecting Schmidt plate," in *Large Ground-based Telescopes* (International Society for Optics and Photonics, 2003), Vol. **4837**, pp. 628–637.
13. R. Goullioud, D. A. Content, G. M. Kuan, J. D. Moore, Z. Chang, E. T. Sunada, and C. A. Powell, "Wide Field Infrared Survey Telescope [WFIRST]: telescope design and simulated performance," Proc. SPIE **8442**, 84421U (2012).
14. M. Borden, D. Lewis, H. Ochoa, L. Jones-Wilson, S. Susca, M. Porter, and B. Netterfield, "Thermal, structural, and optical analysis of a balloon-based imaging system," Publ. Astron. Soc. Pac. **129**, 035001 (2017).